Title

Non-Perturbative Determination of Isotope-induced Anomalous Vibrational Physics.

Journal

Physical Review B (condensed matter and materials physics), 108(14)

ISSN

2469-9950

Authors

Wu, Huan
Qin, Zihao
Li, Suixuan
et al.

Publication Date

2023-10-01

DOI

10.1103/physrevb.108.l140302

Peer reviewed

HHS Public Access

Author manuscript

Phys Rev B. Author manuscript; available in PMC 2024 June 16.

Published in final edited form as:

Phys Rev B. 2023 October ; 108(14): . doi:10.1103/physrevb.108.l140302.

Non-Perturbative Determination of Isotope-induced Anomalous Vibrational Physics

Huan Wu[1], **Zihao Qin**[1], **Suixuan Li**[1], **Lucas Lindsay**[2], **Yongjie Hu**[1,*]

[1]School of Engineering and Applied Science, University of California, Los Angeles, Los Angeles, California 90095, USA

[2]Materials Science and Technology Division, Oak Ridge National Laboratory, Oak Ridge, Tennessee 37831, USA

Abstract

In general, vibrational physics has been well described by quantum perturbation theory to provide footprint characteristics for common crystals. However, despite weak phonon anharmonicity, the recently discovered cubic crystals have shown anomalous vibrational dynamics with elusive fundamental origin. Here, we developed a non-perturbative *ab initio* approach, in together with spectroscopy and high-pressure experiments, to successfully determine the exact dynamic evolutions of the vibrational physics for the first time. We found that the local fluctuation and coupling isotopes significantly dictate the vibrational spectra, through the Brillouin zone folding that has been previously ignored in literature. By decomposing vibrational spectra into individual isotope eigenvectors, we observed both positive and negative contributions to Raman intensity from constitutional atoms (^{10}B, ^{11}B, ^{75}As or ^{31}P). Importantly, our non-perturbative theory predicts that a novel vibrational resonance appears at high hydrostatic pressure due to broken translational symmetry, which was indeed verified by experimental measurement under a pressure up to 31.5 GPa. Our study develops fundamental understandings for the anomalous lattice physics under the failure of quantum perturbation theory and provides a new approach in exploring novel transport phenomena for materials of extreme properties.

Quantum perturbation theory (QPT) is a general approach to describe quantum systems involving phonon, photon, or electron interactions [1,2]. The idea of QPT is to start with a simple system that can be easily solved, and then adding a perturbing Hamiltonian representing a weak disturbance to the system. The complicated systems can therefore be studied based on the knowledge of the simpler one [3,4]. So far, exceptions of QPT only exist in complicated or extreme systems of strong correlations, confinement, anharmonicity, interactions, or bound states [5–20]. For most crystals, the vibrational physics can be well characterized by perturbation theory and thus provide footprint features of their crystal structures [21–23]. However, here we found that in the newly discovered cubic crystals, the coupling and random distribution of isotope atoms breaks the translational symmetry and folds the Brillouin zone, thus the vibration energy cannot be described by perturbation theory [24–30]. To understand the missing phonon physics, we developed a

*Correspondence to: yhu@seas.ucla.edu.

non-perturbative *ab initio* approach to accurately construct the vibrational spectra and enable deterministic predictions matching experimental measurements under controlled isotopes and high pressure.

In literature, QPT has been well applied for simulating vibrational spectra and shown good agreement with experiments for common materials including diamond, Si, Ge, GaAs, InP, AlP, AlSb, AlAs, GaSb, InAs, InSb, SiC, BN, AlN, GaN, etc [21–23,31–64]. In general, each Raman peak is dictated by the vibrational energy corresponding to a phonon branch. However, the recent discovered BAs [24,26–30,64–68] and BP [25] exhibit anomalous Raman spectra evolving between single- and two-modes with isotope stochastic ratio, which does not follow the established understanding and puzzles the field for last several years. Based on the conventional understanding, early studies mistakenly attributed the two Raman peaks to the longitudinal optical (LO) and transverse optical (TO) modes, which was later found to be incorrect because the LO-TO splitting is too small in energy to be observable [25,30,69,70]. Later on, the two modes were naively assigned to isotope vibrations (^{10}B and ^{11}B) simply due to energy proximity, but the fundamental origin is not clear, and the measurement remains to be inconsistent with theory [27,30]. Further experiments [71,72] with tailored isotopes measured the abnormal Raman profiles with transition from single- to two-mode behaviors as a function of isotope stoichiometries, which indicates the isotope disorder is important but can no longer be treated perturbatively. So far, such an anomalous two-mode behavior has not been seen in any other cubic crystals [22]. In the following, we will start by elaborating established models and missing physics in the past literature study, and then proceed to discuss our new development that enables quantitatively understanding of the novel vibrational dynamics.

Many prior studies have considered the disorder effects through QPT [3,4], e.g., treating the isotope interactions as perturbation to a periodic system. Using a mean field perturbation, the eigenmodes or scattering rates can be derived. In particular, under the weak scattering limit, phonon interactions with defects (including isotopes) can be derived from Fermi's golden rule [73] and shows good agreement with the measured phonon linewidths [22]. For increased isotope interactions, the phonon frequency shift due to renormalization can be derived by improving QPT with perturbative quantum field theory [74]. However, fundamentally, all the above perturbative theory frameworks were found to be inadequate for BAs and BP due to their unique atomic structures. We attribute this to two essential missing factors: First, local disorder from randomly distributed isotope atoms can be critical and break the lattice translational symmetry. Second, the coupling interactions between isotope atoms with relatively large mass difference (such as ^{11}B and ^{10}B in BAs or BP) will enable a non-negligible energy splitting for optical phonon modes and thus substantially revise the Hamiltonian from the statistical average or mean field approximation in QPT.

Here, to capture the localized and coupling isotopic vibrational physics in BAs and BP, we develop an *ab initio* approach based on non-perturbative supercell exact diagonalization [75,76] and density functional theory [77,78]. First, we consider the scattering physics of localized isotope disorders as effective folding of the Brillouin zone: In a perfect crystal, atoms are arranged as periodic repetitions of a primitive cell; while for a practical crystal with a mixture of isotopes, isotope atoms could distribute randomly in space and

thus form local disorders to break the original periodicity. Effectively, we treat such a disorder effect as to enlarge the lattice periodicity and fold the Brillouin zone, i.e., additional phonon states will be projected to the Γ point and become assessable for Raman scattering. Exemplary Brillouin zone folding picture is schematically illustrated by the pink shadowed curves in Figure 1a. Second, we explicitly consider the coupling effects from all individual isotope atoms (e.g., ^{10}B, ^{11}B, ^{75}As, ^{31}P) by computing the exact eigenstates from a randomly configured supercell. The importance of such coupling effect in BAs can be gauged from our calculated phonon dispersions for isotopically purely crystals (blue and green dashed curves) in Figure 1a: The energy level splitting between ^{10}BAs and ^{11}BAs is large in comparison with common compounds and phonon linewidths, thus as we expected, the isotope interactions should play an important role in reshaping the vibration spectra. To capture both missing factors from the localized and coupling isotope effects, we form a large supercell with randomly assigned mass for each atom based on isotope concentrations, and then directly diagonalizing the dynamical matrix of the supercell to determine the eigenfrequencies and eigenvectors that captures the exact isotope interactions [79]. The exact eigenfrequencies of the disordered system are obtained non-perturbatively to include energy splitting. The interatomic force constants are determined by *ab initio* approach [80,81] based on density functional theory [77,78] without using fitting parameters or empirical potentials. To ensure an accurate calculation on long-range interatomic interactions within a large supercell, we employ non-local density functionals [82–86] in density functional theory calculations using Quantum ESPRESSSO [87–89]. The interatomic force constants are subsequently extracted by fitting the displacement-force sets using ALAMODE [90]. The dipole-dipole interactions are considered through mixed-space approach [91]. This process is repeated for 1000 randomly generated mass configurations on a supercell with 512 atoms while keeping the interatomic potential same. The final density of state spectra is averaged over the spectra of those mass configurations. Since each mass configuration represents a local snapshot of disorder, the Brillouin zone folding due to translational symmetry breaking is fully considered with a large supercell and multi lattice repetitions. Figure 1b shows the phonon density of states calculated by our non-perturbative supercell exact diagonalization method (red curves), in comparison with virtual crystal approximation (dashed curves): Clearly, a large deviation is observed between the two methods for naturally abundant BAs, verifying our hypothesis that isotope coupling and disorder-induced zone-folding substantially modulate the phonon states.

Next, to determine the exact profile of Raman spectra, we looked at its basic physical process: In a Raman experiment, electron is the media of photon-phonon interaction. Under laser, electrons will oscillate with the external electromagnetic wave, which induces an instantaneous polarization quantified by electrical dipole moment $P^{\mu} = \alpha^{\mu\nu}E^{\nu}$, where $\boldsymbol{E}$ is the electric field, $\boldsymbol{\alpha}$ is the polarizability tensor; μ and ν indicate direction. The light intensity $I(\omega)$ is proportional to the square of the electromagnetic wave amplitude,

$$I(\omega) \propto \left|\hat{\epsilon}_S \cdot \boldsymbol{\alpha}(\omega) \cdot \hat{\epsilon}_I\right|^2 \quad (1)$$

where $\hat{\epsilon}_I$ and $\hat{\epsilon}_S$ are polarization vectors of the incident and scattered light respectively [92,93].

The polarizability tensor can then be expanded as a power series with respect to atomic displacement $\boldsymbol{u}(jl)$,

$$\alpha^{\mu\upsilon} = \alpha_0^{\mu\upsilon} + \alpha_1^{\mu\upsilon} + \cdots \tag{2}$$

where $\alpha_0^{\mu\upsilon} =$ constant ,

$$\alpha_1^{\mu\upsilon} = \sum_{\xi} \sum_{jl} \frac{\partial \alpha^{\mu\upsilon}}{\partial \xi} u_{\xi}(jl) \tag{3}$$

where $\boldsymbol{u}(jl)$ is the atomic displacement of the j^{th} atom in l^{th} cell, and μ, ν, and ξ indicate the direction of the coordinate system. In Eq. (2), the first term corresponds to elastic scattering, and the second term is associated with inelastic scattering due to electron-phonon interactions which contribute to the Raman spectra.

The atomic displacement $\boldsymbol{u}(jl)$ can be treated as the superposition of different modes of lattice waves,

$$\boldsymbol{u}(jl) = \frac{1}{\sqrt{N m_j}} \sum_{\boldsymbol{q}s} \boldsymbol{e}_{\boldsymbol{q}s}(j) \exp(i\boldsymbol{q} \cdot \boldsymbol{r}(jl)) Q_{\boldsymbol{q}s} \tag{4}$$

where $\boldsymbol{q}$ is the phonon wave vector and s is phonon branch; $\boldsymbol{q}s$ labels a certain phonon mode. N is the number of $\boldsymbol{q}$-points in the first Brillouin Zone. m_j and $\boldsymbol{r}(jl)$ are respectively the mass and the equilibrium position of the j^{th} atom in l^{th} cell. $Q_{\boldsymbol{q}s}$ is the normal mode coordinates and gives the amplitude of the lattice wave. $\mathbf{e}_{\boldsymbol{q}s}(j)$ is the eigenvector of the j^{th} atom. By substituting Eq. (4) into Eq. (3), $\boldsymbol{\alpha}_1$ can be expressed in terms of contributions from different phonon modes,

$$\alpha_1^{\mu\upsilon} = \sum_{\boldsymbol{q} \to \boldsymbol{0}, s} \frac{\partial \alpha_{\boldsymbol{q}s}^{\mu\upsilon}}{\partial Q_{\boldsymbol{q}s}} Q_{\boldsymbol{q}s} \tag{5}$$

Here, only optical modes with $\boldsymbol{q} \to \boldsymbol{0}$ contribute to the Raman spectra due to the conservation of energy and momentum in photon-phonon interactions.

Consequently, the Raman intensity at a certain frequency ω is

$$I(\omega) \propto \sum_{S,q\to 0} \frac{\left|\hat{\varepsilon}_S \cdot \frac{\partial \boldsymbol{\alpha}_{qS}}{\partial Q_{qS}} \cdot \hat{\boldsymbol{\varepsilon}}_I\right|^2}{\omega_{qS}} \delta(\omega - \omega_{qS}) \tag{6}$$

For cubic crystals, the crystal symmetry dictates that $\partial\alpha_{\alpha\beta}/\partial u^{\gamma}_{jl} = at_j\epsilon_{\alpha\beta\gamma}$, where a is a constant and $\epsilon_{\alpha\beta\gamma}$ represents the Levi-Civita symbol [94]. For binary compounds, $t_j = 1$ for anions, and $t_j = -1$ for cations. Hence,

$$\frac{\partial \alpha^{\mu\upsilon}}{\partial Q_{qS}} = \sum_{jl} \frac{\partial \alpha^{\mu\upsilon}}{\partial \boldsymbol{u}_{jl}} \frac{\partial \boldsymbol{u}_{jl}}{\partial Q_{qS}} \propto \sum_j t_j \epsilon_{\mu\upsilon\xi} \frac{\left(e^j_{qS}\right)_\xi}{\sqrt{m_j}} \tag{7}$$

When the incident and scattered light are along [111] orientation,

$$I(\omega) \propto \sum_{S,q\to 0} \frac{\left|\sum_{j\xi} t_j \frac{\left(e^j_{qS}\right)_\xi}{\sqrt{m_j}}\right|^2}{\omega_{qS}} \delta(\omega - \omega_{qS}) \tag{8}$$

From Eq. (8), the Raman spectra is mainly determined by the phonon eigenvectors and phonon density of states.

Based on the above *ab initio* supercell exact diagonalization method, we determine the anomalous Raman spectra for BAs and BP varying with isotope concentrations (Figure 2). To verify the calculation results, we chemically synthesized isotopically controlled BAs [27] and BP [25] crystals and performed the Raman measurements. The measured Raman spectra of BAs and BP were obtained from 633 nm wavelength laser excitation with 1200 mm^{-1} grating. We used same laser power and spot size through all measurements in this work to ensure that all samples are exposed under same experimental conditions. Shown in Figure 2a, the Raman spectra by *ab initio* calculation (black dashed curve) are compared with experimental results from our measurement (red dots) and literature [72] (red squares), all showing good agreement. The Raman peaks shift to higher frequency with increasing ^{10}B concentration, as the atoms tend to oscillate faster with smaller mass. The isotopically pure BAs and BP shows only one single Raman peak, but evolves to two-modes under the coupling between different isotopes: For example, in naturally abundant BAs (i.e., with 20.1% ^{10}B concentration) (Figure 2a), a second smaller peak appears at 718.9 cm^{-1}, in addition to its first Raman peak at 700.8 cm^{-1}. With further increased concentration of ^{10}B above 40%, the two peaks gradually move closer to each other, and eventually merge together when ^{10}B is above 80%. For BP, under the natural occurring boron isotope concentration, the second low frequency Raman peak appears at 799.0 cm^{-1}, though with a smaller intensity of about 10% that of the first peak at 827.4 cm^{-1}. With increased ^{10}B concentration, the second peak gradually disappears. Based on our *ab initio* theory and their good agreement with experiment in Figure 2a, such anomalous evolution of Raman spectra

with isotope stoichiometries can be understood from Brillouin zone folding. In the Raman process, only the $\boldsymbol{q} = 0$ modes are active due to the energy and momentum conservation during photon-phonon interactions. For isotopically pure crystals where atomic masses are of perfect periodic distribution, the phonon mode at Γ point forms single Raman peak. Considering the extreme case for example, in amorphous materials, disorders can destroy the periodicity or effectively project all vibrational modes following Brillouin zone folding; as a result, the Raman spectra of amorphous materials resembles the profile of density of states. In comparison, the isotope-mixed BAs and BP are mass disordered lattice with partial phonon modes folded to Γ point and become accessible to Raman spectra. Further, we compare the results between the supercell exact diagonalization approach and the virtual crystal approximation. As shown in Figure 2b, virtual crystal result (black dashed curve) is always limited to a single Raman peak and is almost linearly changing with the ^{10}B fraction. Our *ab initio* results, on the other hand, shows a non-linearity due to the evolutions from single peak to coupled two peaks, in consistent with experimental observation. Essentially, the localized isotope vibrations and their coupling deviate from the calculations based on homogenous virtual atoms.

Importantly, our study indicates that each individual Raman peak involves substantial contributions from all isotope vibration modes, which means the respective Raman peak could be assigned to the separate vibrational behaviors of two boron isotopes, i.e., ^{10}B- and ^{11}B-like behaviors. To quantitatively understand the coupled contributions to each Raman peak observed in the natural BAs and BP, we decompose the Raman intensity contribution among all constitutional atoms (i.e, all isotopes of B, As or P) based on their eigenvectors. For As and P, a single isotope ^{75}As, and ^{31}P dominates the natural abundance respectively. The contribution of Raman intensity from each isotope is determined following Eq. (9):

$$I^X(\omega) \propto \sum_{s,q\to 0} W_{qs}^X \frac{\left|\sum_{j\xi} t_j \frac{(e_{qs}^j)_\xi}{\sqrt{m_j}}\right|^2}{\omega_{qs}} \delta(\omega - \omega_{qs}) \tag{9}$$

where X could be ^{10}B, ^{11}B, ^{75}As, and ^{31}P. W_{qs}^X is the weighting factor of each isotope,

$$W_{qs}^X = \frac{\sum_{j\in X,\xi} \frac{(e_{qs}^j)_\xi}{\sqrt{m_j}}}{\sum_{j\xi} \frac{(e_{qs}^j)_\xi}{\sqrt{m_j}}} \tag{10}$$

As shown in Figure 3, we quantify the total Raman spectra (black solid curve) from respective contributions by each isotope (color dashed curve): ^{10}B, ^{11}B, ^{75}As or ^{31}P. A prior naïve understanding is that the high frequency peak corresponds to the ^{10}B-like mode, and the low frequency peak correspond to the ^{11}B-like mode. However, from Figure 3, all isotopes show non-negligible contributions to each Raman peak, due to the strong coupling between ^{10}B and ^{11}B as discussed above. The interatomic forces between the atomic pairs in the system affect all isotopes and collectively determine the oscillation

frequency. Essentially, our study indicates that the coupling from two isotope modes plays important role in re-shaping the Raman spectral profile.

Another interesting finding based on our calculations is that a negative contribution to total Raman intensity could exist from a certain isotope mode. For example, for BP in Figure 3b, at the low frequency peak, there is −3.7% contribution from ^{10}B when ^{10}B concentration is 20%, which indicates the ^{10}B and ^{11}B has opposite directions of eigenvector based on Eq. (9) and (10), so that ^{10}B mode destructively contributes to the total Raman intensity. To elucidate further, when the ^{10}B mode originally at Brillouin zone edge, folds back to the Brillouin zone center, it gives a negative contribution to Raman intensity due to the opposite eigenvector and overlapped frequency compared with the ^{11}B mode at Brillouin zone center. However, the negative contribution is not obvious for BAs, because in BAs the optical frequencies at Brillouin zone edge is far away from the frequencies at Γ point.

Moreover, we exemplify the power of the *ab initio* approach by high pressure study. Based on the developed *ab initio* theory, we expect that under high pressures, a resonance shoulder will appear on the lower frequency side of the ^{11}B TO peak in naturally abundant BAs. From Eq. (8), the Raman intensity is not only affected by the density of states, but also the alignment and magnitude of the eigenvectors. Therefore, this prediction of new resonance shoulder can be understood by looking at the alignment function of the eigenvectors in a specific direction z, which we define as:

$$\eta_z = \left(\sum_j \frac{t_j (e^j_{qs})_z}{\sqrt{m_j}} \right)^2 \tag{11}$$

The larger value of η_z indicates better alignment on vibrational. If the eigenvector directions of each atom are randomly distributed, the positive and negative values of $(e^j_{qs})_z$ cancel with each other, and then η_z becomes zero. When η_z reaches a peak value, the corresponding phonon modes allows high probability for atoms to have synchronous vibrations, i.e., forming a resonance shoulder in Raman spectra. Based on the *ab initio* theory, η_z is calculated under varied hydrostatic pressures. As shown in Figure 4a, η_z shift towards higher energy from ambient pressure (yellow) to high pressure (red). In addition, the high pressure reshapes the η_z profile: a local peak for η_z evolves at 815 cm^{-1} under 31.5 GPa (pointed circle, Figure 4a). For this enhanced eigenvector alignment at 815 cm^{-1} under 31.5 GPa, our *ab initio* calculations (black solid curve, Figure 4b) predict that an abnormal resonance Raman shoulder will appear at the same position. To verify our prediction, we performed in-situ Raman experiment under high hydrostatic pressure using a diamond anvil cell setup [24,79] as illustrated in Figure 4c. BAs single crystal sample was loaded in diamond anvil cell (Figure 4d). In Figure 4b, the experimental results (red dot) are compared with *ab initio* theory predictions (black solid curve). The experiment shows an evolved resonance shoulder in the Raman spectra (pointed circle) under high pressure: For example, it appears at 775 cm^{-1} for 22.3 GPa and moving further to 815 cm^{-1} for 31.5 GPa, in good agreement with theory prediction (black curve). The experimental observation of such unique features

in high-pressure Raman spectra further verified the modeling accuracy based on *ab initio* theory.

In summary, we investigated the vibrational modes in high thermal conductivity BAs and BP crystals and quantitively determined the physics origin of the anomalous vibrational modes through the comparison between *ab initio* theory and experiment indicates. We developed *ab initio* calculations based on density functional theory and non-perturbative supercell exact diagonalization method to determine the profiles of Raman spectra under varied isotope stoichiometry that shows good agreement with experimentally measurements. Our study found that the dynamic evolution of Raman spectra with isotope stoichiometries can be quantitatively explained by the coupling between all constitutional atoms and the translational symmetry breaking induced by local isotope mass inhomogeneity. By decomposing the Raman insensitivity to each eigenvector of constitutional atoms (e.g., ^{10}B, ^{11}B, ^{75}As, ^{31}P), we clarified that each Raman peak is contributed collectively from all vibrational modes rather than from single mode, while both constructive and destructive coupling exist. In addition, an abnormal vibrational shoulder is theoretically predicted at high pressure due to breaking of translational symmetry in BAs and experimentally verified by our high-pressure experiment. This study exemplifies the power of combining *ab initio* theory and experiment in exploring new transport phenomena for materials with extreme properties [68,95].

Acknowledgments.

Y.H. acknowledges support from CAREER Award from the National Science Foundation (NSF) under Grant No. DMR-1753393, Alfred P. Sloan Research Fellowship under Grant No. FG-2019-11788, and Vernroy Makoto Watanabe Excellence in Research Award. This work used computational and storage services associated with the Hoffman 2 Shared Cluster provided by UCLA Institute for Digital Research and Education's Research Technology Group, and the Bridges-2 at Pittsburgh Supercomputing Center through allocation DMR180111 from Extreme Science and Engineering Discovery Environment, which was supported by National Science Foundation grant number 1548562.

References

[1]. Ashcroft NW and Mermin ND, Solid State Physics (Holt, Rinehart and Winston, New York, 1976).

[2]. Ziman JM, Principles of the Theory of Solids (Cambridge University Press, 1972).

[3]. Sakurai JJ, Modern Quantum Mechanics (Addison-Wesley Publishing Company, 1994).

[4]. Mahan GD, Many- Particle Physics (Kluwer, 2000).

[5]. Tang HK, Leaw JN, Rodrigues JNB, Herbut IF, Sengupta P, Assaad FF, and Adam S, The role of electron-electron interactions in two-dimensional Dirac fermions, Science 361, 570 (2018). [PubMed: 30093594]

[6]. Paschen S and Si Q, Quantum phases driven by strong correlations, Nat. Rev. Phys 3, 9 (2021).

[7]. Altshuler BL, Gefen Y, Kamenev A, and Levitov LS, Quasiparticle lifetime in a finite system: a nonperturbative approach, Phys. Rev. Lett 78, 2803 (1997).

[8]. Dombi P, Pápa Z, Vogelsang J, V Yalunin S, Sivis M, Herink G, Schäfer S, Groß P, Ropers C, and Lienau C, Strong-field nano-optics, Rev. Mod. Phys 92, 025003 (2020).

[9]. Souvatzis P, Eriksson O, Katsnelson MI, and Rudin SP, Entropy driven stabilization of energetically unstable crystal structures explained from first principles theory, Phys. Rev. Lett 100, 095901 (2008). [PubMed: 18352725]

[10]. Errea I, Rousseau B, and Bergara A, Anharmonic stabilization of the high-pressure simple cubic phase of calcium, Phys. Rev. Lett 106, 165501 (2011). [PubMed: 21599380]

[11]. Tadano T and Tsuneyuki S, Self-consistent phonon calculations of lattice dynamical properties in cubic $SrTiO_3$ with first-principles anharmonic force constants, Phys. Rev. B 92, 054301 (2015).

[12]. Skelton JM et al. , Anharmonicity in the high-temperature *Cmcm* phase of SnSe: Soft modes and three-phonon interactions, Phys. Rev. Lett 117, 075502 (2016). [PubMed: 27563974]

[13]. Kang JS, Wu H, Li M, and Hu Y, Intrinsic low thermal conductivity and phonon renormalization due to strong anharmonicity of single-crystal tin selenide, Nano Lett. 19, 4941 (2019). [PubMed: 31265307]

[14]. Bazavov A et al. , Nonperturbative QCD simulations with *2+1* flavors of improved staggered quarks, Rev. Mod. Phys 82, 1349 (2010).

[15]. Briceño RA, Dudek JJ, and Young RD, Scattering processes and resonances from lattice QCD, Rev. Mod. Phys 90, 025001 (2018).

[16]. Huber MQ, Nonperturbative properties of Yang–Mills theories, Phys. Rep 879, 1 (2020).

[17]. Levinson YB and Rashba EI, Electron-phonon and exciton-phonon bound states, Rep. Prog. Phys 36, 1499 (1973).

[18]. Zhu J, Badalyan SM, and Peeters FM, Electron-phonon bound states in graphene in a perpendicular magnetic field, Phys. Rev. Lett 109, 256602 (2012). [PubMed: 23368485]

[19]. Camacho-Guardian A, Bastarrachea-Magnani MA, and Bruun GM, Mediated interactions and photon bound states in an exciton-polariton mixture, Phys. Rev. Lett 126, 017401 (2021). [PubMed: 33480782]

[20]. Thébaud S, Polanco CA, Lindsay L, and Berlijn T, Success and breakdown of the T-matrix approximation for phonon-disorder scattering, Phys. Rev. B, 102 094206 (2020).

[21]. Baroni S, de Gironcoli S, Dal Corso A, and Giannozzi P, Phonons and related crystal properties from density-functional perturbation theory, Rev. Mod. Phys 73, 515 (2001).

[22]. Cardona M and Thewalt MLW, Isotope effects on the optical spectra of semiconductors, Rev. Mod. Phys 77, 1173 (2005).

[23]. Srivastava GP, The Physics of Phonons (CRC Press, 1990).

[24]. Li S, Qin Z, Wu H, Li M, Kunz M, Alatas A, Kavner A, and Hu Y, Anomalous thermal transport under high pressure in boron arsenide, Nature 612, 459 (2022). [PubMed: 36418403]

[25]. Kang JS, Wu H, and Hu Y, Thermal properties and phonon spectral characterization of synthetic boron phosphide for high thermal conductivity applications, Nano Lett. 17, 7507 (2017). [PubMed: 29115845]

[26]. Kang JS, Li M, Wu H, Nguyen H, and Hu Y, Basic physical properties of cubic boron arsenide, Appl. Phys. Lett 115, 122103 (2019).

[27]. Kang JS, Li M, Wu H, Nguyen H, and Hu Y, Experimental observation of high thermal conductivity in boron arsenide, Science 361, 575 (2018). [PubMed: 29976798]

[28]. Li S, Zheng Q, Lv Y, Liu X, Wang X, Huang PY, Cahill DG, and Lv B, High thermal conductivity in cubic boron arsenide crystals, Science 361, 579 (2018). [PubMed: 29976796]

[29]. Tian F et al. , Unusual high thermal conductivity in boron arsenide bulk crystals, Science 361, 582 (2018). [PubMed: 29976797]

[30]. Hadjiev VG, Iliev MN, Lv B, Ren ZF, and Chu CW, Anomalous vibrational properties of cubic boron arsenide, Phys. Rev. B 89, 024308 (2014).

[31]. Herchen H and Cappelli MA, First-order Raman spectrum of diamond at high temperatures, Phys. Rev. B 43, 11740 (1991).

[32]. Anastassakis E, Hwang HC, and Perry CH, Temperature dependence of the long-wavelength optical phonons in diamond, Phys. Rev. B 4, 2493 (1971).

[33]. Lang G, Karch K, Schmitt M, Pavone P, Mayer AP, Wehner RK, and Strauch D, Anharmonic line shift and linewidth of the Raman mode in covalent semiconductors, Phys. Rev. B 59, 6182 (1999).

[34]. Zhang JM, Giehler M, Göbel A, Ruf T, Cardona M, Haller EE, and Itoh K, Optical phonons in isotopic Ge studied by Raman scattering, Phys. Rev. B 57, 1348 (1998).

[35]. Menéndez J and Cardona M, Temperature dependence of the first-order Raman scattering by phonons in Si, Ge, and α-Sn: Anharmonic effects, Phys. Rev. B 29, 2051 (1984).

[36]. Debernardi A, Baroni S, and Molinari E, Anharmonic phonon lifetimes in semiconductors from density-functional perturbation theory, Phys. Rev. Lett 75, 1819 (1995). [PubMed: 10060399]

[37]. Cardona M and Ruf T, Phonon self-energies in semiconductors: anharmonic and isotopic contributions, Solid State Commun. 117, 201 (2001).

[38]. Irmer G, Wenzel M, and Monecke J, The temperature dependence of the LO(T) and TO(T) phonons in GaAs and InP, Phys. Stat. Sol (b) 195, 85 (1996).

[39]. Debernardi A, Phonon linewidth in III-V semiconductors from density-functional perturbation theory, Phys. Rev. B 57, 12847 (1998).

[40]. Giannozzi P, de Gironcoli S, Pavone P, and Baroni S, *Ab initio* calculation of phonon dispersions in semiconductors, Phys. Rev. B 43, 7231 (1991).

[41]. Mooradian A and Wright GB, First order Raman effect in III–V compounds, Solid State Commun. 4, 431 (1966).

[42]. Lindsay L, Broido DA, and Reinecke TL, *Ab initio* thermal transport in compound semiconductors, Phys. Rev. B 87, 165201 (2013).

[43]. Vallée F, Time-resolved investigation of coherent LO-phonon relaxation in III-V semiconductors, Phys. Rev. B 49, 2460 (1994).

[44]. Beer SZ, Jackovitz JF, Feldman DW, and Parker JH, Raman and infrared active modes of aluminium phosphide, Phys. Lett. A 26, 331 (1968).

[45]. Azuhata T, Sota T, and Suzuki K, Second-order Raman spectra and lattice dynamics in AlAs, J. Phys.: Condens. Matter 7, 1949 (1995).

[46]. Raptis YS, Anastassakis E, and Kanellis G, Second-order Raman scattering in AlSb, Phys. Rev. B 46, 15801 (1992).

[47]. Wagner J, Fischer A, Braun W, and Ploog K, Resonance effects in first- and second-order Raman scattering from AlAs, Phys. Rev. B 49, 7295 (1994).

[48]. Aoki K, Anastassakis E, and Cardona M, Dependence of Raman frequencies and scattering intensities on pressure in GaSb, InAs, and InSb semiconductors, Phys. Rev. B 30, 681 (1984).

[49]. Leite RCC and Scott JF, Resonant Surface Raman Scattering in Direct-Gap Semiconductors, Phys. Rev. Lett 22, 130 (1969).

[50]. Carles R, Saint-Cricq N, Renucci JB, Renucci MA, and Zwick A, Second-order Raman scattering in InAs, Phys. Rev. B 22, 4804 (1980).

[51]. Kiefer W, Richter W, and Cardona M, Second-order Raman scattering in InSb, Phys. Rev. B 12, 2346 (1975).

[52]. Karch K, Pavone P, Windl W, Schütt O, and Strauch D, *Ab initio* calculation of structural and lattice-dynamical properties of silicon carbide, Phys. Rev. B 50, 17054 (1994).

[53]. Lysenko V, Barbier D, and Champagnon B, Stress relaxation effect in porous 3C-SiC/Si heterostructure by micro-Raman spectroscopy, Appl. Phys. Lett 79, 2366 (2001).

[54]. Feldman DW, Parker JH, Choyke WJ, and Patrick L, Phonon Dispersion Curves by Raman Scattering in SiC, Polytypes *3C*, *4H*, *6H*, *15R*, and *21R*, Phys. Rev 173, 787 (1968).

[55]. Reich S, Ferrari AC, Arenal R, Loiseau A, Bello I, and Robertson J, Resonant Raman scattering in cubic and hexagonal boron nitride, Phys. Rev. B 71, 205201 (2005).

[56]. Karch K and Bechstedt F, *Ab initio* lattice dynamics of BN and AlN: Covalent versus ionic forces, Phys. Rev. B 56, 7404 (1997).

[57]. Bungaro C, Rapcewicz K, and Bernholc J, *Ab initio* phonon dispersions of wurtzite AlN, GaN, and InN, Phys. Rev. B 61, 6720 (2000).

[58]. Perlin P, Polian A, and Suski T, Raman-scattering studies of aluminum nitride at high pressure, Phys. Rev. B 47, 2874 (1993).

[59]. Brafman O, Lengyel G, Mitra SS, Gielisse PJ, Plendl JN, and Mansur LC, Raman spectra of AlN, cubic BN and BP, Solid State Commun. 6, 523 (1968).

[60]. McNeil LE, Grimsditch M, and French RH, Vibrational spectroscopy of aluminum nitride, J. Am. Ceram. Soc 76, 1132 (1993).

[61]. Filippidis L, Siegle H, Hoffmann A, Thomsen C, Karch K, and Bechstedt F, Raman frequencies and angular dispersion of polar modes in aluminum nitride and gallium nitride, Phys. Stat. Sol (b) 198, 621 (1996).

[62]. Miwa K and Fukumoto A, First-principles calculation of the structural, electronic, and vibrational properties of gallium nitride and aluminum nitride, Phys. Rev. B 48, 7897 (1993).

[63]. Ulrich C, Debernardi A, Anastassakis E, Syassen K, and Cardona M, Raman linewidths of phonons in Si, Ge, and SiC under pressure, Phys. Stat. Sol (b) 211, 293 (1999).

[64]. Yang X, Feng T, Kang JS, Hu Y, Li J, and Ruan X, Observation of strong higher-order lattice anharmonicity in Raman and infrared spectra, Phys. Rev. B 101, 161202(R) (2020).

[65]. Lindsay L, Broido DA, and Reinecke TL, First-principles determination of ultrahigh thermal conductivity of boron arsenide: A competitor for diamond?, Phys. Rev. Lett 111, 025901 (2013). [PubMed: 23889420]

[66]. Kang JS, Li M, Wu H, Nguyen H, Aoki T, and Hu Y, Integration of boron arsenide cooling substrates into gallium nitride devices, Nat. Electron 4, 416 (2021).

[67]. Cui Y, Qin Z, Wu H, Li M, and Hu Y, Flexible thermal interface based on self-assembled boron arsenide for high-performance thermal management, Nat. Commun 12, 1284 (2021). [PubMed: 33627644]

[68]. Cui Y, Li M, and Hu Y, Emerging interface materials for electronics thermal management: experiments, modeling, and new opportunities, J. Mater. Chem. C 8, 10568 (2020).

[69]. Solozhenko VL, Kurakevych OO, Le Godec Y, V Kurnosov A, and Oganov AR, Boron phosphide under pressure: In situ study by Raman scattering and X-ray diffraction, J. Appl. Phys 116, 33501 (2014).

[70]. Zheng Q, Li S, Li C, Lv Y, Liu X, Huang PY, Broido DA, Lv B, and Cahill DG, High thermal conductivity in isotopically enriched cubic boron phosphide, Adv. Funct. Mater 28, 1805116 (2018).

[71]. Sun H, Chen K, Gamage GA, Ziyaee H, Wang F, Wang Y, Hadjiev VG, Tian F, Chen G, and Ren Z, Boron isotope effect on the thermal conductivity of boron arsenide single crystals, Mater. Today Phys 11, 100169 (2019).

[72]. Rai A, Li S, Wu H, Lv B, and Cahill DG, Effect of isotope disorder on the Raman spectra of cubic boron arsenide, Phys. Rev. Mater 5, 013603 (2021).

[73]. Tamura S, Isotope scattering of dispersive phonons in Ge, Phys. Rev. B 27, 858 (1983).

[74]. Mahan GD, Effect of atomic isotopes on phonon modes, Phys. Rev. B 100, 024307 (2019).

[75]. Dean P, The vibrational properties of disordered systems: Numerical studies, Rev. Mod. Phys 44, 127 (1972).

[76]. Dove MT and Dove MT, Introduction to Lattice Dynamics (Cambridge university press, 1993).

[77]. Hohenberg P and Kohn W, Inhomogeneous electron gas, Phys. Rev 136, B864 (1964).

[78]. Kohn W and Sham LJ, Self-consistent equations including exchange and correlation effects, Phys. Rev 140, A1133 (1965).

[79]. See Supplementary Materials at https://journals.aps.org/prl/ for details.

[80]. Wu H, Fan H, and Hu Y, *Ab initio* determination of ultrahigh thermal conductivity in ternary compounds, Phys. Rev. B 103, L041203 (2021).

[81]. Fan H, Wu H, Lindsay L, and Hu Y, *Ab initio* investigation of single-layer high thermal conductivity boron compounds, Phys. Rev. B 100, 085420 (2019).

[82]. Thonhauser T, Cooper VR, Li S, Puzder A, Hyldgaard P, and Langreth DC, Van der Waals density functional: Self-consistent potential and the nature of the van der Waals bond, Phys. Rev. B 76, 125112 (2007).

[83]. Lee K, Murray ÉD, Kong L, Lundqvist BI, and Langreth DC, Higher-accuracy van der Waals density functional, Phys. Rev. B 82, 081101(R) (2010).

[84]. Berland K, Cooper VR, Lee K, Schröder E, Thonhauser T, Hyldgaard P, and Lundqvist BI, Van der Waals forces in density functional theory: a review of the vdW-DF method, Rep. Prog. Phys 78, 066501 (2015). [PubMed: 25978530]

[85]. Cooper VR, Van der Waals density functional: An appropriate exchange functional, Phys. Rev. B 81, 161104 (2010).

[86]. Klimeš J, Bowler DR, and Michaelides A, Van der Waals density functionals applied to solids, Phys. Rev. B 83, 195131 (2011).

[87]. G. P and B. S and B. N and C. M and C. R and C. C and C. D and L. C. G and C. M and D. I and D. C. A and de G. S and Wentzcovitch SF, QUANTUM ESPRESSO: a modular and open-source software project for quantum simulations of materials, J. Phys.: Condens. Matter 21, 395502 (2009). [PubMed: 21832390]

[88]. Giannozzi P et al. , Advanced capabilities for materials modelling with Quantum ESPRESSO, J. Phys.: Condens. Matter 29, 465901 (2017). [PubMed: 29064822]

[89]. Giannozzi P et al. , Quantum ESPRESSO toward the exascale, J. Chem. Phys 152, 154105 (2020). [PubMed: 32321275]

[90]. Tadano T, Gohda Y, and Tsuneyuki S, Anharmonic force constants extracted from first-principles molecular dynamics: applications to heat transfer simulations, J. Phys.: Condens. Matter 26, 225402 (2014). [PubMed: 24824156]

[91]. Wang Y, Wang JJ, Wang WY, Mei ZG, Shang SL, Chen LQ, and Liu ZK, A mixed-space approach to first-principles calculations of phonon frequencies for polar materials, J. Phys.: Condens. Matter 22, 202201 (2010). [PubMed: 21393699]

[92]. Born M and Bradburn M, The theory of the Raman effect in crystals, in particular rock-salt, Proc. R. Soc. Lond. A 188, 161 (1947).

[93]. Hayes W and Loudon R, Scattering of Light by Crystals (John Wiley and Sons, 1978).

[94]. Baroni S, de Gironcoli S, and Giannozzi P, Phonon dispersions in $Ga_xAl_{1-x}As$ alloys, Phys. Rev. Lett 65, 84 (1990). [PubMed: 10042178]

[95]. Li M, Dai L, and Hu Y, Machine learning for harnessing thermal energy: From materials discovery to system optimization, ACS Energy Lett. 7, 3204 (2022). [PubMed: 37325775]

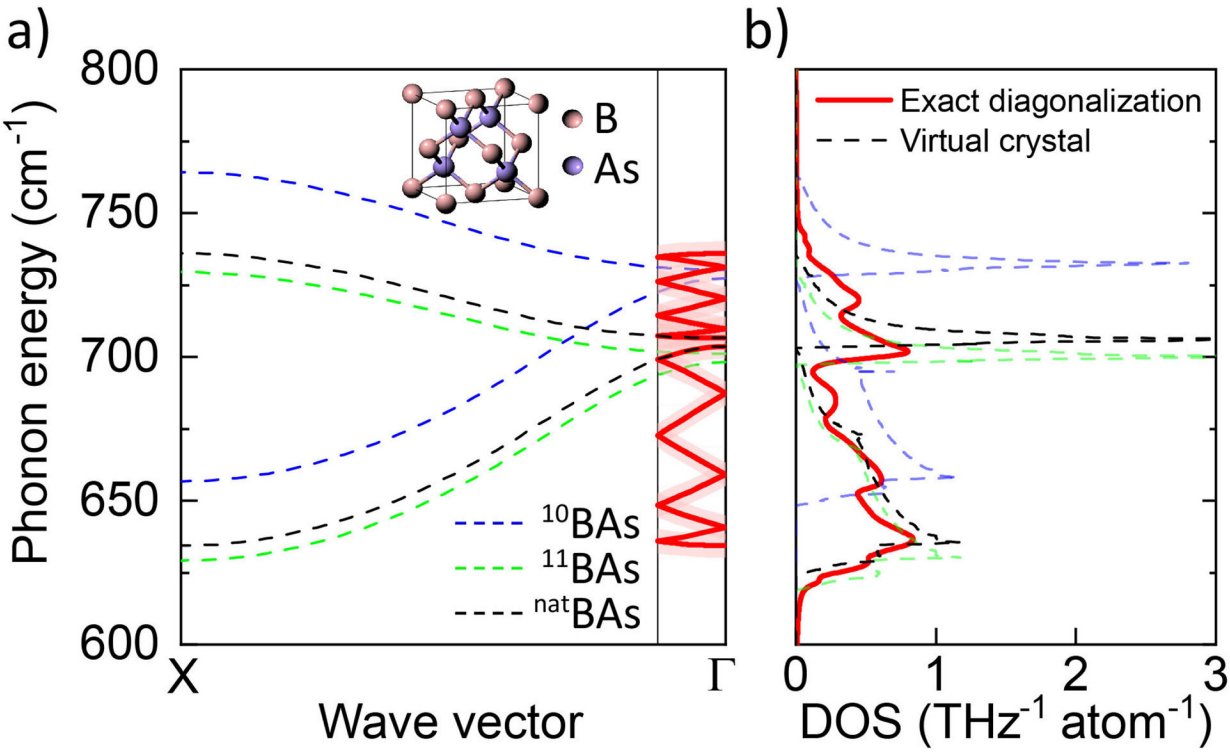

Figure 1. Brillouin zone folding and translational symmetry breaking due to local fluctuation and coupling of distributed isotope atoms.

(a) Phonon band structures (optic branches) for isotopically pure and naturally abundant BAs. Schematic in the right column (red shadow), illustrating an example of Brillouin zone folding due to local and coupled isotope effects. (b) Phonon density of states (DOS) calculated by different model methods. The DOS of naturally abundant BAs is determined by the supercell exact diagonalization theory (red solid curve) to include the prior missing contributions from local isotope disorders and their coupling, showing clear differences from the virtual crystal calculation (black dashed curve). The comparison indicates a substantial redistribution of phonon states due to isotope effects of Brillouin zone folding and energy splitting.

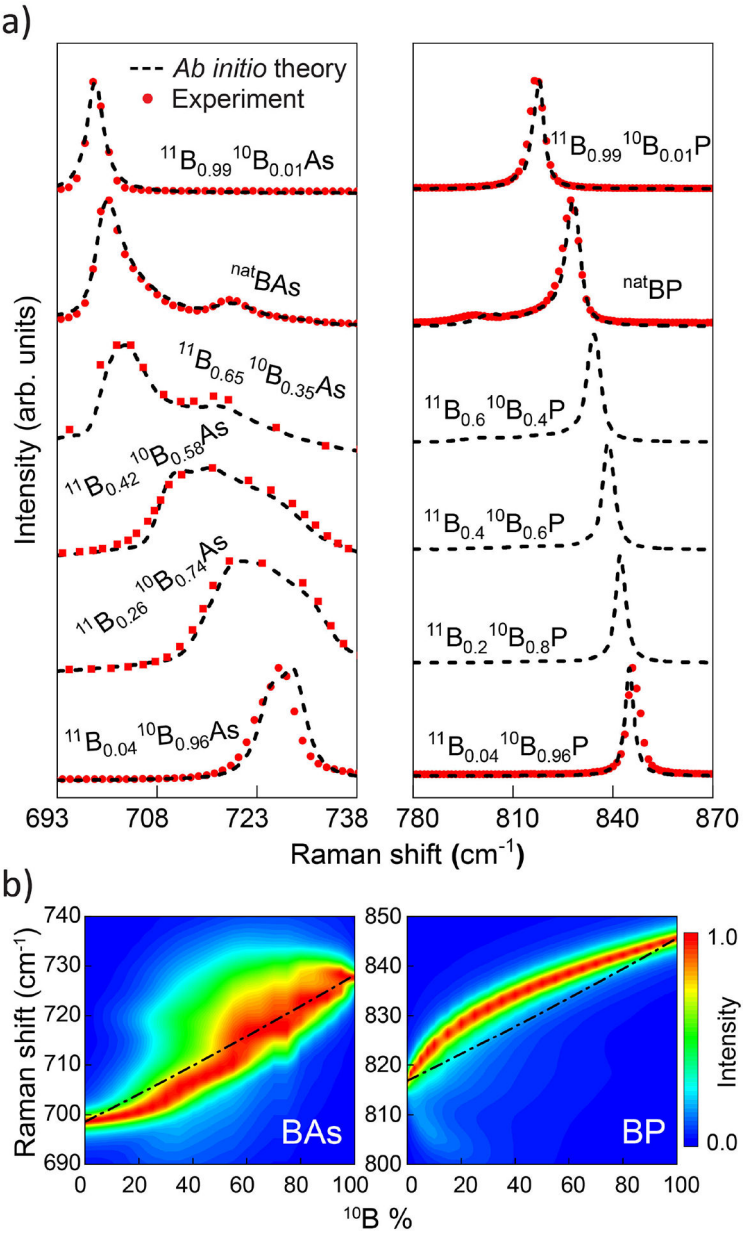

Figure 2. Quantitative profile-determination of vibrational dynamics by *ab initio* theory in comparison with experimental measurements, under varying isotope concentrations.

(a) The dynamic evolution of Raman spectra with different isotope stichometry concentrations between ^{10}B and ^{11}B for (a) BAs and (b) BP. The Raman spectral profiles determined by *ab initio* calculation based on the supercell exact diagonalization theory (black dashed curve), considering the local isotope vibrations and their coupling, are in good agreement with experimental data from our measurement (red dot) and literature (red square) [72]. (b) The *ab initio* theory determined Raman spectra is plotted in two-dimensional color map, illustrating the broaden of Raman spectra and evolution from single-mode to two-mode behaviors due to isotope coupling. Plotted for comparison, is the virtual crystal approximation (dashed curve), indicating its limitation to single mode and failure to capture the coupling physics in these boron compounds.

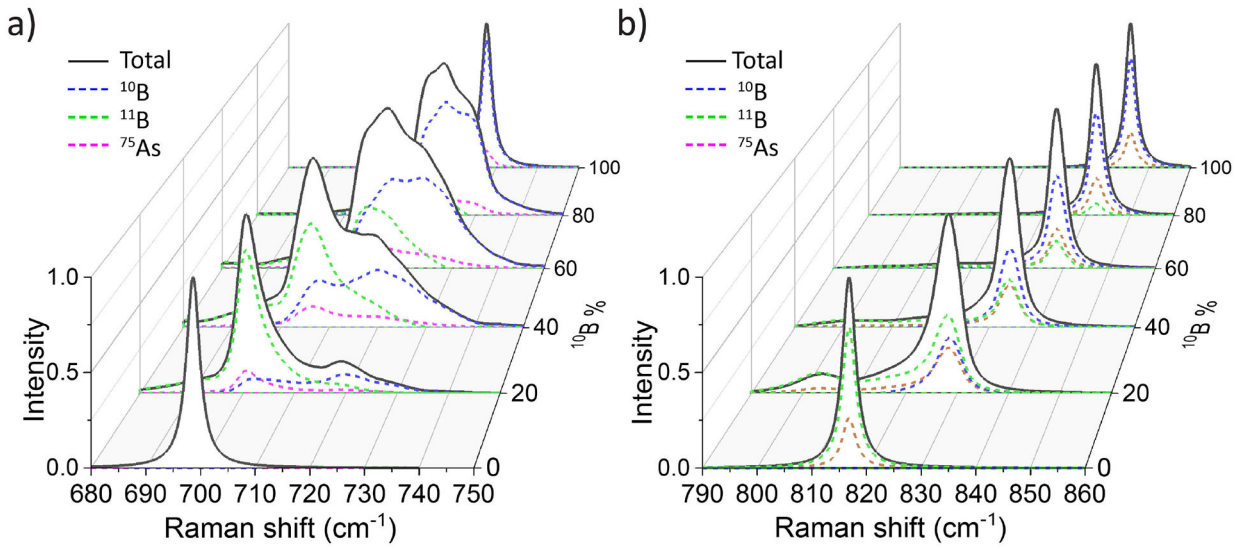

Figure 3. Decomposition of vibrational spectra into constitutional atomic modes by tracing the eigenvectors.

The Raman intensity for (a) BAs and (b) BP under varied isotope concentrations, are decomposed into respective contributions of ^{10}B, ^{11}B, ^{75}As or ^{31}P. The total Raman spectra (black solid curve) is a summation of all isotope contributions (dashed) and shows good agreement with experiments in Figure 2. Negative contribution is observed from individual isotope mode, e.g., ^{10}B mode in $^{10}B_{0.2}{}^{11}B_{0.8}P$.

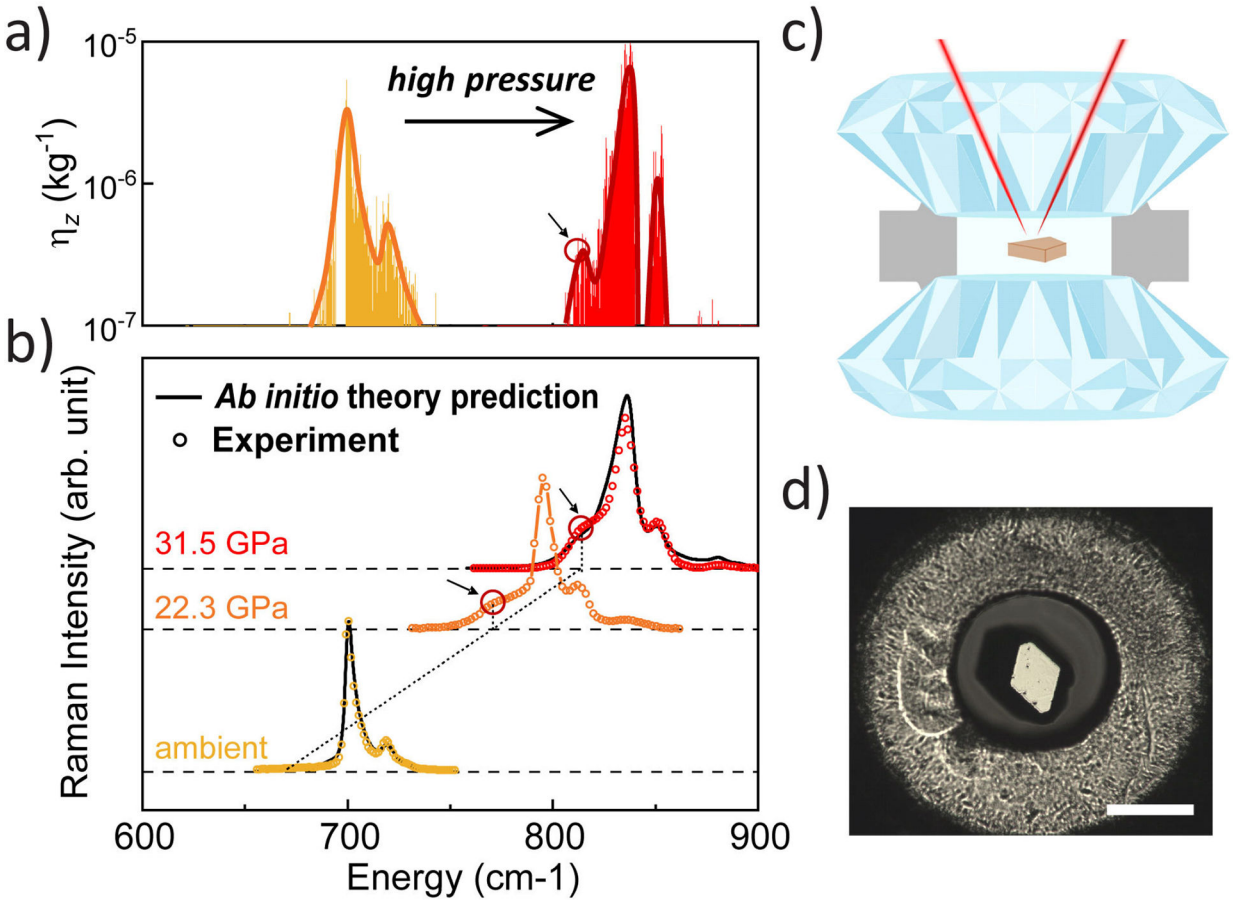

Figure 4. Abnormal vibrational resonance shoulder for ^{nat}BAs under high pressure predicted by *ab initio* theory and verified by experiment.

(a) The calculated alignment function η_z at ambient (orange yellow column) and high pressure (red column), predicting an evolving η_z peak at high pressure that facilitate Raman scattering near its shoulder. The profile of η_z is illustrated by solid curves. (b) Comparison between the theory prediction (black curve) and experimental measurement (red dot) of Raman spectra under ambient and high pressures, verifying the appearance of a new shoulder (highlighted by red circle and arrow). (c) Experimental setup of diamond anvil cell for in situ Raman measurement under high pressure. (d) Image of BAs sample loaded inside the diamond anvil cell. Scale bar is 100 μm.